On the Microstructural Origin of Brain White Matter Hydraulic Permeability

Marco Vidotto[a,b], **Andrea Bernardini**[b], **Marco Trovatelli**[c], **Elena De Momi**[a], and **Daniele Dini**[b,1]

[a]Department of Electronics, Information and Bioengineering, Politecnico di Milano, Milano, 20133 Italy; [b]Department of Mechanical Engineering, Imperial College London, London, SW7 2AZ United Kingdom; [c]Department of Health, Animal Science and Food Safety, Faculty of Veterinary Medicine, University of Milan, Milan, Italy

Brain microstructure plays a key role in driving the transport of drug molecules directly administered to the brain tissue as in Convection-Enhanced Delivery procedures. The proposed research analyses the hydraulic permeability of two white matter (WM) areas (corpus callosum and fornix) whose three-dimensional microstructure was reconstructed starting from the acquisition of electron microscopy images. We cut the two volumes with 20 equally spaced planes distributed along two perpendicular directions and, on each plane, we computed the corresponding permeability vector. Then, we considered that the white matter structure is mainly composed of elongated and parallel axons and, using a principal component analysis, we defined two principal directions, parallel and perpendicular with respect to the axons' main direction. The latter were used to define a new reference frame onto which projecting the permeability vectors to finally obtain the permeability along the parallel and perpendicular directions. The results show a statistically significant difference between parallel and perpendicular permeability, with a ratio about 2 in both the white matter structures analysed, thus demonstrating their anisotropic behaviour. Moreover, we find a significant difference between permeability in corpus callosum and fornix which suggests that also the white matter heterogeneity should be considered when modelling drug transport in the brain. Our findings, that demonstrate and quantify the anisotropic and heterogeneous character of the white matter, represent a fundamental contribution not only for drug delivery modelling but also for shedding light on the interstitial transport mechanisms in the extracellular space.

Brain Tissue | Hydraulic Permeability | Convection-Enhanced Delivery | Computational Fluid Dynamics (CFD) | Imaging

Understanding the effect of the brain microstructure on spatial drug distribution is pivotal to design effective treatment strategies for neurological disorders (1).

The recent introduction of an innovative technique called Convection-Enhanced Delivery (CED) in the neurosurgical scenario opened up the possibility to deliver chemotherapeutic agents to brain tumours and, more recently, gene therapy for Parkinson's disease and antiseizure agents for epilepsy (2–4). In CED, the main idea is to use convection to augment the local concentration of a drug by directly infusing in the brain tissue (5). Usually, one or more catheters are stereotactically placed in the region of interest and then anchored to a pump that can inject a drug at certain flow rate, which is usually in the order of $\mu l/min$ (6). Using CED, it is possible to achieve a much higher spatial distribution of the drug because the pressure gradient allows infusing over a larger volume with respect to other methods (5).

Despite CED has shown promising results in the field of neurological drug delivery, clinical trials did not succeed in demonstrating benefit in terms of life expectancy for patients (5–7). Indeed, for CED to be effective, it is necessary to have a sufficiently high concentration of drug in the regions occupied by the diseased tissue. However, a number of factors such as catheter design, catheter placement and infusion protocol, which are often very difficult to control, influence the drug distribution and concentration profile. Accordingly, clinicians would significantly benefit from making use of numerical models able to predict the drug distribution and concentration in the preoperative phase (5, 6). A predictive model allows the surgeon to test different scenarios in terms of catheter setup and infusion settings in the preoperative phase to decide the best way to operate on the patient.

Although several models devoted to tackle the above scenario have been developed in the last 20 years (8–12), there are still important discrepancies between prediction and reality, thus suggesting the need for more refined and comprehensive approaches (1). In particular, the brain extracellular space (ECS) spatial organisation is identified as a pivotal factor for drug transport as highlighted by (13). However, there exists only a limited number of studies which have tried to understand the relation between ECS and hydraulic permeability, a fundamental parameter for modelling CED, which is also the subject of an important controversy (14, 15).

Recent advance in imaging and 3D reconstruction of brain structures at the cellular level have laid the first milestone towards a deeper understanding of the ECS spatial organisation role. For example, (14) used the neuropil reconstruction (grey matter) by (16) to compare advective and diffusive transport within the interstitial space. Tools have also been developed

Significance Statement

Unveiling the mechanisms that drive the mass transport in the brain tissue is fundamental, not only to plan accurate surgical procedures but also to shed light on the way solutes move in the extracellular space during physiological or pathological state. The relation between the white matter spatial organisation and relevant parameters such as permeability is still an unsolved question. Here we simulate the interstitial flow between the axons of two white matter areas reconstructed through 3D electron microscopy imaging. We show that the permeability computed parallel to the axons is significantly higher than the one calculated perpendicularly and that corpus callosum exhibits a higher permeability than fornix, hence demonstrating the importance of the anisotropic and heterogeneous behaviour of WM.

www.pnas.org/cgi/doi/10.1073/pnas.XXXXXXXXXX

PNAS | July 29, 2021 | vol. XXX | no. XX | 1–7

(17) to perform a detailed analysis of other fibrous soft tissues, such as those developed to study the meniscus microstructure, in which the fluid flows during the transmission of the load to the articular cartilage, and to link the local tissue microstructure to the zonal variation of elastic and viscoelastic properties of the tissue (18).

In this work, we use the dataset obtained using focused ion beam scanning electron microscopy (FIB-SEM) to provide 2D and 3D tissue microstructural information, as provided by (19), to examine the permeability of two white matter (WM) structures, corpus callosum (CC) and fornix (FO). By integrating the information acquired simulating a convective flow between the axons and the principal component analysis (PCA) performed on the axons' centerline, we determine and, in doing so, confirm the ability to predict the strongly anisotropic character of the WM in terms of hydraulic permeability. Moreover, comparing the two WM structures, we reveal the significant difference between different WM areas. The relations between ECS and WM anisotropy and heterogeneity are here systematically discussed for the first time and represent an important contribution not only for CED modelling but also for understanding interstitial solute transport.

Results

This study was conducted starting from the dataset provided by (19), who reconstructed the 3D volume of brain areas by means of FIB-SEM. This method offers some advantages with respect to other electron microscopy techniques, the most important being the capability of scanning an entire volume by sequentially ablating layers of the specimen. This feature is especially important when dealing with WM, whose strongly anisotropic geometrical organisation is well known (20). Indeed, it allows avoiding issues related to the registration of consecutive images in order to obtain an accurate 3D reconstruction.

Figure 1 briefly outlines the main steps of this work. In Figure 1A, two different cuts are shown: the coronal cut exposes the CC whereas the sagittal cut exposes the FO. A sample from each anatomical area was harvested, fixed, stained and imaged with the FIB-SEM (Figure 1B) as described in (19). From each volume, we selected 20 equally spaced slices (10 parallel to the xy plane and 10 parallel to the xz plane Figure 1B), where we manually segmented the axons boundary. Indeed, although automatic segmentation methods have shown incredible performances for the morphometry of WM structures, these are usually employed to image the intracellular space rather than the ECS (21–23). In these scenarios, small errors may not play a major role in the accuracy of the reconstruction of the domain of interest. On the contrary, since in this study we focus on the relation between ECS and permeability, we preferred to perform a manual segmentation thus avoiding unrealistic intersections of close axons, which are extremely important for the exact determination of flow, as suggested also in (16).

Finally, an example section from the CC parallel to the xy plane is shown in Figure 1C with a detail of the discretised surface. As described in *Methods*, the resulting mesh, that contains more than 600,000 elements, is the result of a sensitivity analysis. Note that, each slice has an ECS volume fraction of about 30%, which is within the physiological range (24) (Table 1).

Table 1. Average ECS volume fraction and standard deviation for the xy plane and the xz plane of CC and FO.

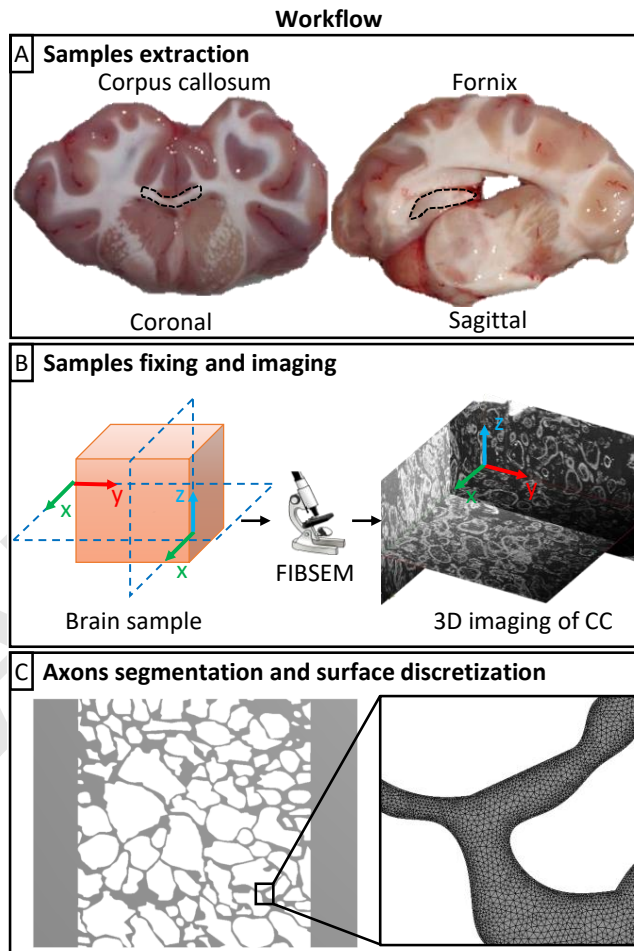| WM region	xy plane	xz plane
CC	0.31 ± 0.019	0.33 ± 0.022
FO	0.27 ± 0.049	0.28 ± 0.038

Workflow

Fig. 1. Workflow outline A) A coronal and a sagittal cut were performed on a sheep brain. These cuts exhibit two WM regions, CC and FO, from which two samples were harvested (as highlighted by the dashed black contour). B) The WM samples were fixed, stained and imaged by means of a FIB-SEM with a resolution of 0.02 $\mu m/px$ as detailed in (19) C) The 3D volumes of CC and FO were divided in 20 equally spaced slices (10 parallel to the xy plane and 10 parallel to the xz plane) where the axons boundaries were manually selected. A detail of the triangular discretisation performed on each slice (about 300000 elements) can be appreciated in the inset exploded in the right part of the figure.

Flow and pressure. The velocity and pressure fields were computed by solving the Navier-Stokes equations with ANSYS Fluent (ANSYS, Lebanon, NH). The boundary conditions were chosen according to the literature on CED (15): we imposed a velocity of 0.0025 m/s at the inlet and a pressure of 0 Pa at the outlet, modelling the axons as impermeable and rigid bodies (14). Note that, since the brain is usually considered an hyperelastic tissue, the last assumption is valid only with very low flow rate because the deformations, caused by the applied pressure, can be considered negligible (10, 12).

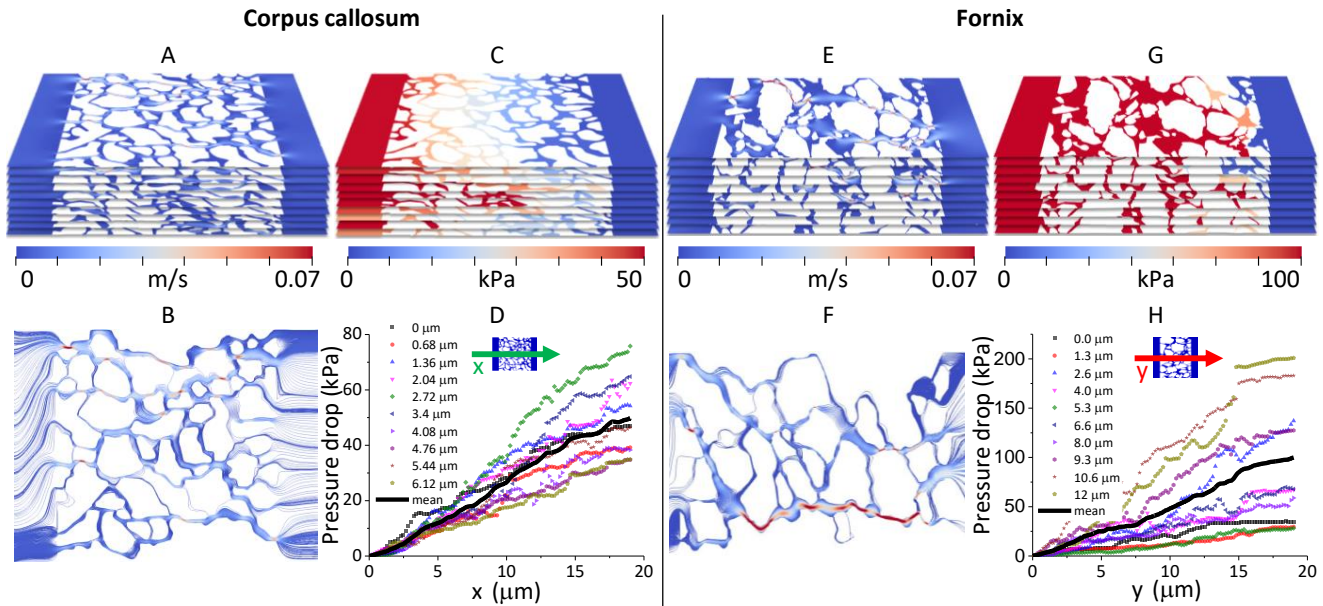Figure 2 shows the results of the numerical analysis con-

Corpus callosum ... **Fornix**

Fig. 2. These results have been obtained applying a velocity of 0.0025 m/s at the inlet and a pressure of 0 Pa at the outlet as boundary conditions. A) Contour of the x component of the velocity in the CC. B) Velocity streamlines computed on a cross-section of the CC at depth equal to 3.4 μm. C) Pressure contours on the xy planes of the CC. D) Pressure drop along the x direction on each slice of the CC. The black line indicates the mean value that increases linearly ($R^2 \approx 0.99$) from 0 to 50 kPa. E) Contour of the y component of the velocity in the FO. F) Velocity streamlines computed on a cross-section of the FO at depth equal to 8 μm. G) Pressure contours on the xy planes of the FO. H) Pressure drop along the y direction on each slice of the FO. The black line indicates the mean value that increases linearly ($R^2 \approx 0.99$) from 0 to 100 kPa.

ducted on the 2D slices extracted from CC and FO. Looking at the velocity profile, CC and FO show similar results with a maximum velocity around 0.07 m/s (Figure 2 A and E). Moreover, we can detect some of the features found in the topological analysis on a rat CA1 hippocampal neuropil performed by (16), where the authors divided the ECS into tunnels and sheets. The first are formed at the junction of three or more cells and have a 40 - 80 nm diameter, whereas the second can be found between pairs of cells with a width of 10 - 40 nm. Despite the brain samples being taken from WM areas and not neuropil, we can still recognise a similar topological organisation which has an impact on the velocity profile. Indeed, the velocity increases, especially, in the sheets between axons, as it is possible to recognise in the streamlines depicted in Figure 2 B and F.

On the other hand, Figures 2 C and G show that the pressure decreases from inlet to outlet as the flux encounters greater local pressure loss due to the tortuous geometry of the ECS. Moreover, comparing the pressure loss across CC and FO, we notice that in the FO the pressure required to allow a convective flux is about twice that required in the CC. This could be due to the greater presence of axons with a larger equivalent diameter in the FO with respect to the CC. Indeed, this kind of axons are expected to offer higher resistance to the flux with respect to the smaller ones. Despite this difference, in both CC and FO the pressure drop increases linearly ($R^2 \approx$ 0.99) along the length of the samples as shown in Figures 2 D and H. The black line represents the average pressure drop along the x and y axes for CC and FO, respectively.

Similar results, not displayed here for the sake of brevity, were found also in the other planes.

Parallel and perpendicular directions. As outlined in the introduction, the main aim of this manuscript is to show how the strongly anisotropic geometry of the WM influences a

fundamental parameter for drug delivery, namely hydraulic permeability. In the proposed work, coherently with other researchers (10, 12, 25), we considered the WM a transversely isotropic porous medium defined by a principal direction parallel to the axons and a perpendicular plane in which the material's behaviour is direction-independent. As a consequence, we can summarise our objective in the definition of the parallel permeability ($k_\parallel$) and the perpendicular permeability ($k_\perp$).

To this end, in each plane, we considered the WM as an homogeneous porous material, where the pressure loss and the average velocity through the pores are linearly related by Darcy's law (26, 27). As a consequence, we were able to compute 10 different permeability tensors $\mathbf{k^{xyz}}$ with respect to the FIB-SEM imaging reference frame xyz (Fig. 3A). However, since xyz is randomly oriented, these preliminary results need to be rotated in order to be expressed with respect to a more informative reference frame taking into account the WM principal directions.

To do that, at first we perform a PCA on the centerline of each axon (19, 28) and then, by averaging the first component of the PCA, we identify the overall parallel direction Z (Fig. 3A). Subsequently, randomly choosing two of the infinite vectors orthogonal to Z, we define the XYZ reference frame, where X and Y lie on the plane perpendicular to the axons. Figure 3A is an example showing the CC but the same operation is performed also on the FO. Indeed, as it can be inferred from Figure 3B, CC and FO exhibit a different orientation of the principal directions with respect to the imaging reference frame xyz.

Then, using the Euler angles, it is possible to express each permeability tensor $\mathbf{k^{xyz}}$ with respect to the XYZ reference frame thus obtaining the $\mathbf{k^{XYZ}}$ tensors and, consequently, 10 values of k_X, k_Y and k_Z (Fig. 3C). Finally, $k_\parallel$ coincides with
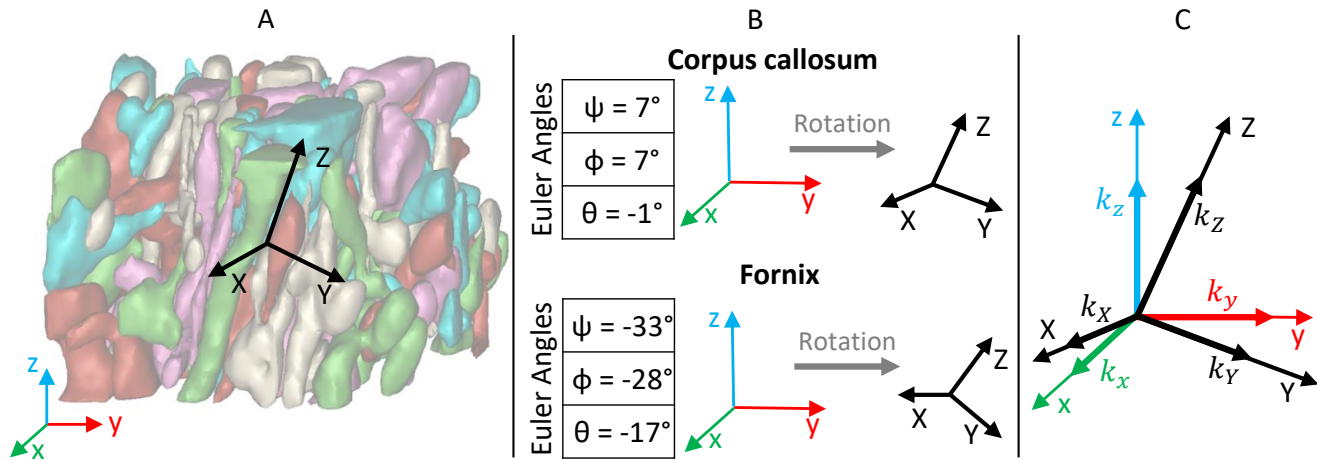
Fig. 3. A) Three-dimensional volume of the CC reconstructed by Bernardini et al. (19) with respect to the FIBSEM imaging reference frame xyz. On the contrary, since the WM geometrical organisation is strongly anisotropic, the XYZ reference frame (in black) is defined according to the WM principal directions: the Z axis is parallel to the axons whereas X and Y are two vectors chosen randomly to form a right-handed coordinate system. B) The Euler angles ψ, ϕ and θ, which express the intrinsic rotation about the x, y and z axes, respectively, describe the orientation of the XYZ reference frame with respect to the xyz reference frame. C) Both the xyz and the XYZ reference frames are centred in the origin: k_x, k_y and k_z are the x, y and z components of the permeability tensor $\mathbf{k}$. The latter is then expressed with respect to the XYZ reference frame by means of the Euler angles. As a consequence, k_X k_Y and k_Z are given by the sum of the contribution of the k_x, k_y and k_z vectors along the X, Y and Z axes, respectively.

k_Z whereas $k_\perp$ is obtained averaging k_X and k_Y. Details of the computation are reported in the *Methods* section.

Permeability. For the CC, $k_\parallel$ is comprised between 1,046 and 2,249 nm^2 with a median value of 1,710 nm^2. The results obtained along the same direction but for the FO are considerably lower with a median value of 907 nm^2 and ranging from 429 to 1,777 nm^2.

On the other hand, looking at the perpendicular direction, in the CC $k_\perp$ is equal to 794, 525 and 1,049 nm^2 for the median, minimum and maximum values respectively. Even in the perpendicular direction, the FO exhibits permeability values lower than CC: the median of $k_\perp$ is about 432 nm^2 and values range between 210 and 716 nm^2. We analysed these results by looking at two aspects: the first is related to the WM anisotropy that we expect to influence the hydraulic permeability, whereas the second aims at understanding if also the anatomical area from which the samples have been harvested plays an important role.

To this end, since the Shapiro-Wilk tests on $k_\parallel$ and $k_\perp$ rejected normality for both CC and FO ($p < 0.10^{-3}$), we conducted a statistical analysis using the Mann-Whitney rank-sum test for unpaired samples.

The analysis results are summarised in Figure 4. In both white matter areas, the comparison between $k_\parallel$ and $k_\perp$ shows a statically significant difference ($p = 2.46 \cdot 10^{-4}$ for CC and $p = 0.0028$ for FO). This outcome strongly suggests that the anisotropic geometrical organisation of the WM has an impact on the flow across the tissue which ultimately leads to different values of permeability. It also interesting to note that the ratio between the median value of $k_\parallel$ and $k_\perp$ is comparable in the two WM samples analysed: 2.15 in the CC and 2.09 in the FO.

Moreover, we inspect the WM by comparing the permeability values in the same direction obtained in the CC and FO samples. Also in this case the Mann-Whitney rank-sum test was used. As shown in Figure 4, for both $k_\parallel$ and $k_\perp$, there is statistically significant difference between the two samples ($p = 0.0022$ for $k_\parallel$ and $p = 0.0028$ for $k_\perp$). This result clearly represents a measure of the heterogeneity of the WM in different regions of the brain.
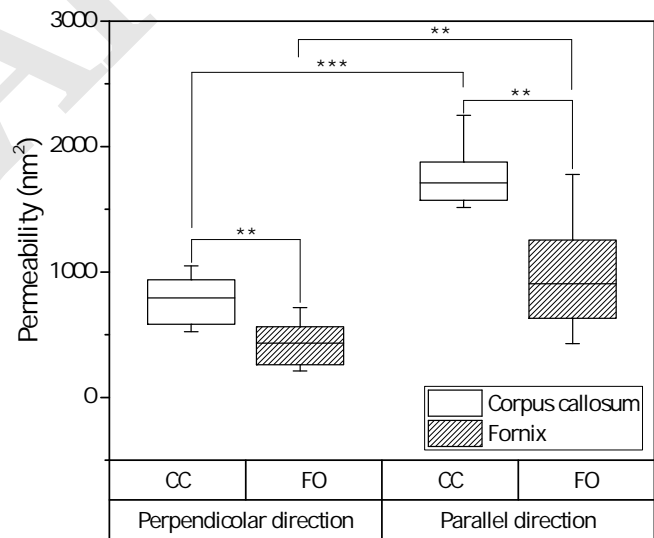

Fig. 4. The boxplot shows a comparison between permeability evaluated on CC and FO taking into account the WM anisotropy and the anatomical area from which were harvested. The statistical analysis, conducted with the Mann-Whitney rank-sum test for unpaired samples demonstrates that there is a strong statistical difference between $k_\parallel$ and $k_\perp$ in the CC ($p = 2.46 \cdot 10^{-4}$) and between $k_\parallel$ and $k_\perp$ in the FO ($p = 0.0028$). Moreover, we find evidences of a statistically significant difference also comparing the $k_\parallel$ in CC and FO ($p = 0.0022$) and the $k_\perp$ in CC and FO ($p = 0.0028$).

Discussion

Most of the research efforts of the last 20 years to address the need for tool to predict the drug distribution profile in the brain, were conducted by implementing more and more complex mathematical models (8–12). However, despite previous

cited investigations represent extremely valuable contributions, they still do not guarantee a sufficient level of accuracy because of the large uncertainty on most of the constitutive parameters. Indeed, as pointed out by (13), the ECS is still a largely unknown territory made of narrow intercellular channels which form very tortuous paths.

It is only recently that new microscopy imaging techniques have started to unveil the real structure of the ECS thus giving the possibility to run accurate numerical simulations (14, 16). In this manuscript, we exploit the 3D reconstruction of two WM structures from (19), namely CC and FO, to reach three objectives: quantify the hydraulic permeability, highlight its anisotropic behaviour and show the zonal heterogeneity of within the WM.

Quantifying the brain hydraulic permeability has always represented a very challenging problem that has been addressed following two main approaches, experimental and numerical. Just a few works have followed the experimental approach, with (29, 30) who performed their experiments on human and lamb brain tissue respectively, whereas (31) used cerebral neoplastic tissue. Very recently, (32) quantified for the first time the influence of directionality of axonal structures on permeability of WM of fresh ovine brain tissue by directly measuring the response to infusion of specimens excised from the corona radiata (CR).

Table 2. Comparison of permeability values from the literature.

Tissue Type	Permeability (nm^2)	Approach	Ref
Sheep CC $k_\perp$	794	N	This study
Sheep FO $k_\perp$	432	N	This study
Sheep CC $k_\parallel$	1,710	N	This study
Sheep FO $k_\parallel$	907	N	This study
Human/lamb brain tissue	24.7	E	(29, 30)
U87 human glioblastoma	487	E	(31)
$k_\perp$ from WM model	$122 - 133$	N	(15)
WM human	7,500	N	(33)
Ovine CR perpendicular	70	E	(32)
Ovine CR parallel	200	E	(32)

E and N stand for experimental and numerical approach respectively. A viscosity of $1 mPa \cdot s$ was assumed when the permeability was converted from hydraulic conductance (15)

The results, summarised in Table 2 shows that our permeability values are much higher than the one found by Franceschini et al. and Tavner et al. (29, 30). However, in the comparison, we need to consider a fundamental difference: our research focuses specifically on WM areas whereas Franceschini et al. and Tavner et al. considered a generic brain tissue sample (with either white and grey matter and without considering the directionality in the tissue). Accordingly, their value can be only considered representative of an isotropic and homogeneous sample of the brain. Despite this issue prevents a convincing comparison, the fact that the ratio between their result and ours is roughly one order of magnitude recalls the ratio that it is usually found in the literature between grey matter (isotropic tissue) and WM (anisotropic tissue) (11, 33, 34).

On the other hand, our outcomes are in the same order of magnitude of the research conducted by Netti et al. (31). In this work, the authors first performed a series of confined compression tests on excised tissue of human glioblastoma (U87) and then they fitted the experimental data with a poro-viscoelastic model. Note that, as suggested by Tavner et al. (30), there is still an important debate on which model is the most appropriate for brain tissue. In this case, we can only speculate that the similarity between our findings is probably due to the fact that the porous structure of the U87 cell line is somehow similar to the WM, thus offering a comparable resistance to the flow.

Furthermore, an interesting comparison is offered by the experimental work recently presented in (32), demonstrated the importance of local microstructural features, in terms of directionality of the axons, on hydraulic permeability of WM. Their work confirms the conclusions drawn by the present research showing the fundamental role of the anisotropic structural organisation of the WM. It should also be noted that the permeability values measured in (32) are lower than ours; there are important differences with respect to our work that may explain the quantitative discrepancies in terms of permeability values. First of all, in (32) a different region of the brain is analysed, which has an obvious impact on the results, as also demonstrated in our work. Moreover, localised expansion and associated local deformation of the WM induced by the infusion experiments performed in (32) to probe the brain tissue may also be responsible for the reported discrepancy in values.

A second approach is represented by numerical studies. Basser et al. (33) developed a geometrical model based on important simplifying assumptions. The resulting permeability in the WM is probably overestimated and does not include any anisotropic property. On the contrary, Vidotto et al. (15) implemented an idealised geometrical model of the WM in the perpendicular direction starting from the axon diameter distribution from (35). Looking at Table 2, we can notice that our results in the perpendicular direction are in good agreement with their work.

From this overview, it is clear that a proper comparison with the state of the art is not possible because our work represents the first computational, systematic and comprehensive analysis of the WM permeability considering the directionality of the axons in two WM areas. Indeed, in Figure 4, we show that there is a statistically significant difference between permeability in the parallel and perpendicular direction in both CC and FO. To the best of our knowledge, this research demonstrates, for the first time, the anisotropic properties of the WM starting from the reconstructed microstructure of the axonal fibres. This represents a step change with respect to magnetic resonance imaging based method, such as diffusion tensor imaging (DTI) or neurite orientation dispersion and density imaging (NODDI) (36). Indeed, despite DTI and NODDI are fundamental tools used in the standard clinical practice, they usually have a resolution in the order of millimetres whereas the average ECS width is in tens of nanometres (24). Therefore, they can only provide macroscopic and homogenised information about the WM microstructure and, in turn, about the permeability.

Furthermore, we provide a quantitative estimate of the ratio between $k_\parallel$ and $k_\perp$ that, in both CC and FO, is about 2. Obviously, we cannot claim that this ratio is constant across the brain but it suggests that a ratio equal to 10 or more, which is found in several CED modelling works (10, 12), may

₃₃₈ be overestimated.

₃₃₉ Also, our findings provide a clear picture of the WM hetero-
₃₄₀ geneity within a single animal (Fig. 4). Considering both $k_\parallel$
₃₄₁ and $k_\perp$, there is, indeed, a statically significant difference be-
₃₄₂ tween CC and FO. This proves not only that the brain cannot
₃₄₃ be easily divided in grey and white matter, but also that simply
₃₄₄ dividing all WM according to the parallel and perpendicular
₃₄₅ preferential direction of the axons is not enough to provide a
₃₄₆ pointwise-accurate description of the tissue. Therefore, also
₃₄₇ this aspect deserves a further in-depth analysis.

₃₄₈ In this study the solid components of the brain tissue are
₃₄₉ modelled as rigid. However, this hypotheses is valid only for
₃₅₀ low flow rate and it and care must be taken when higher flow
₃₅₁ rates need to be considered or in case of dynamic loading under
₃₅₂ e.g. traumatic brain injury, for which more comprehensive
₃₅₃ models, including the effect of the deformation of the solid
₃₅₄ constituents and an accurate description of their viscoelas-
₃₅₅ tic nature, may be required (37). Nonetheless, our research
₃₅₆ lays the groundwork for future studies, in which the brain
₃₅₇ solid phase deformation could be considered by changing the
₃₅₈ baseline values obtained assuming rigid axons as a function of
₃₅₉ loading and deformations (11).

₃₆₀ It must also be noted that the resolution of the features
₃₆₁ characterizing the axonal wall geometry and its roughness
₃₆₂ is limited by the resolution of the FIB-SEM images. While
₃₆₃ higher resolution could be reached by enhancing the FIB-SEM
₃₆₄ resolution and the computational power associated with the
₃₆₅ resulting finer FEM meshes, here a compromise was made
₃₆₆ to avoid prohibitive imaging and computing times. While
₃₆₇ smoothing of the axons boundaries helps the process by avoid-
₃₆₈ ing mesh irregularities and improving the description of the
₃₆₉ wall, the application of the method to low flow rates also
₃₇₀ ensures that potential deviations from the exact description
₃₇₁ of the flow near the axons arising from not capturing the wall
₃₇₂ roughness beyond the resolution achieved in the reconstruction
₃₇₃ are negligible. This will also need to be reconsidered when
₃₇₄ larger flow rates and deformable surfaces come into play.

₃₇₅ Finally, it should be emphasised that while our study anal-
₃₇₆ ysed brain tissue from a single animal, the work performed by
₃₇₇ Bernardini and co-workers (19), used to obtain the images in
₃₇₈ the present contribution, has recently provided an extended
₃₇₉ dataset (available as a separate repository on Zenodo (38))
₃₈₀ comprising three ovine brains sampled in three different areas
₃₈₁ of the cerebral tissue. The authors of (19) have also shown
₃₈₂ that the features obtained from multiple images obtained from
₃₈₃ one sample are in principle able to provide a statistically
₃₈₄ significant description of similar areas of WM from other sam-
₃₈₅ ples obtained from the same or different animals. The use
₃₈₆ of the extended dataset and further data becoming available
₃₈₇ through similar studies will give the opportunity to increase
₃₈₈ the robustness of the findings in future studies.

₃₈₉ To conclude, in the absence of advanced experimental tech-
₃₉₀ niques capable of determining the dependence of hydraulic
₃₉₁ permeability on tissue microstructure in different areas of
₃₉₂ WM, our study provides an important step forward in the
₃₉₃ assessment of such property starting from the reconstruction
₃₉₄ of axonal structures based on FIB-SEM images. We must
₃₉₅ underline that the importance of our findings is not limited to
₃₉₆ drug delivery but may have consequences also for the some-
₃₉₇ what controversial discussion on interstitial solute transport
₃₉₈ in the ECS (14, 39) and for the validation of models aimed at

₃₉₉ assessing the effect of micro-structural features starting from
₄₀₀ the DTI analysis (36).

Materials and Methods

Finite-Elements Simulations. The brain is modelled as a porous ₄₀₃
medium in which fluxes of molecules, drugs or cerebrospinal fluid ₄₀₄
take place in the interstitial space between the axons. The latter ₄₀₅
represent the solid phase of the white matter that, for very low flow ₄₀₆
rate, can be considered as a rigid material (10, 12, 15). Accordingly, ₄₀₇
the flow is modelled by the Stokes equations (27): ₄₀₈

$$\mu \Delta \mathbf{v} - \nabla p = 0 \qquad [1]$$

$$\nabla \cdot \mathbf{v} = 0 \qquad [2]$$

where $\mathbf{v}$ is the fluid velocity, p the pressure and μ the viscosity (10^{-3} ₄₁₂
$Pa \cdot s$). As boundary conditions, we imposed a velocity equal to ₄₁₃
0.0025 m/s at the inlet and 0 Pa pressure at the outlet with a no slip ₄₁₄
condition on the axon walls ($\mathbf{v} = 0$) as suggested in other studies (15). ₄₁₅
The resulting partial differential equations were solved in the finite ₄₁₆
element method (FEM) software ANSYS (ANSYS, Lebanon, NH) ₄₁₇
with semi-implicit method for pressure linked equations (SIMPLE). ₄₁₈
The meshes were generated using ANSYS meshing tool. Generating ₄₁₉
a mesh and running a simulation took about 60 minutes on an ₄₂₀
Intel i7-6800K processor. For both samples, we analysed 10 equally ₄₂₁
spaced slices parallel to the FIB-SEM xy plane and 10 slices parallel ₄₂₂
to the xz plane (Figure 1B). ₄₂₃

Mesh sensitivity analysis. The ECS of the WM shows a highly tor- ₄₂₄
tuous and intricate ramification of channels that makes the dis- ₄₂₅
cretisation process very challenging. To ensure that the results ₄₂₆
are independent from the meshing parameters, we performed a ₄₂₇
mesh sensitivity analysis varying the elements size on the edges and ₄₂₈
the maximum face size. The mesh was refined 7 times going from ₄₂₉
67,000 triangular elements for the baseline to 760,000 triangular ₄₃₀
elements for the finest mesh. We stopped refining the mesh when ₄₃₁
the difference between two consecutive mesh refinements in term of ₄₃₂
both average velocity and pressure drop was below 1%. Accordingly, ₄₃₃
the final mesh used to compute the flux in all the geometries has the ₄₃₄
following parameters: element size on the edges equal to 0.015 μm ₄₃₅
and maximum face size of the triangles equal to 0.045 μm for a total ₄₃₆
elements number around 600,000 (Figure 1C). Note that, meshing ₄₃₇
biological structures is intrinsically very challenging or it may even ₄₃₈
be impossible if considering the entire 3D volume reconstruction ₄₃₉
from the imaging dataset. In such cases, more robust approaches, ₄₄₀
such as those described in (40) and (41), would be advisable. ₄₄₁

Permeability. The hydraulic permeability of a porous media can be ₄₄₂
computed using Darcy's law which describes the linear relation ₄₄₃
between pressure drop and velocity (15, 27): ₄₄₄

$$\tilde{\mathbf{v}} = \frac{\mathbf{k}}{\mu} \nabla p \qquad [3]$$

where $\mathbf{k}$ and ∇p are the hydraulic permeability and the pressure ₄₄₆
gradient in the direction of the flux, respectively, and $\tilde{\mathbf{v}}$ is the ₄₄₇
velocity through the pores averaged on the fluid volume according ₄₄₈
to the following equation: ₄₄₉

$$\tilde{\mathbf{v}} = \frac{1}{V} \int_{V_f} \mathbf{v} dV \qquad [4]$$

where V and V_f are the total and fluid volume respectively (15, 42). ₄₅₁
Using Eq. 3 and Eq. 4, we computed the permeability values in ₄₅₂
the FIBSEM imaging reference frame (xyz) thus obtaining, for each ₄₅₃
sample, 10 values of k_x, k_y and k_z, namely the diagonal elements ₄₅₄
of 10 different $\mathbf{k^{xyz}}$ tensors (Figure 2). ₄₅₅

Then, to describe the WM permeabilty with respect to a more ₄₅₆
informative set of coordinates, we defined the XYZ reference frame. ₄₅₇
To do that, we first conducted a PCA on the axons' centerline thus ₄₅₈
obtaining, for each one of them, a vector indicating the principal ₄₅₉
direction (Z_i^{PCA}). Next, we performed a weighted average between ₄₆₀

the Z_i^{PCA} vectors to find the overall principal direction (Z), using the following equation:

$$Z = \frac{\sum_{i=1}^{N} L_i * Z_i^{PCA}}{\sum_{i=1}^{N} L_i} \quad [5]$$

Where N is the total number of axons and L_i is the linear length of the ith axon defined as the euclidean distance from head to tail. In this way, we gave more importance to the longer axons, namely the one occupying a larger portion of the volume.

Assuming that the WM can be modelled as a transversely isotropic porous medium (10, 12, 43), we randomly chose the X and Y vectors to form the right-handed reference frame XYZ where Z and XY represent the directions parallel and orthogonal to the axons, respectively. The orientation of the XYZ reference frame with respect to the xyz reference frame can be described by means of the Euler angles ψ, ϕ and θ expressing the intrinsic rotation about the x, y and z axes. Then, with simple trigonometric operations, we converted the Euler angles in the corresponding rotation matrix (R_{XYZ}^{xyz}) and we expressed each one of the previously computed permeability tensors $\mathbf{k^{xyz}}$ with respect to the XYZ reference frame:

$$\mathbf{k^{XYZ}} = (R_{XYZ}^{xyz})^{-1} \cdot \begin{bmatrix} k_x & 0 & 0 \\ 0 & k_y & 0 \\ 0 & 0 & k_z \end{bmatrix} \quad [6]$$

Finally, summing the X, Y and Z components of each $\mathbf{k^{XYZ}}$ tensor, we computed 10 values of k_X, k_Y and k_Z. Since k_X and k_Y lie on the same plane, we calculated $k_\perp$ as the mean value between them whereas $k_\parallel$ coincides with k_Z. Note that, all the operations listed above were conducted for both CC and FO independently.

1. E Vendel, V Rottschäfer, EC de Lange, The need for mathematical modelling of spatial drug distribution within the brain. *Fluids Barriers CNS* **16**, 12 (2019).
2. W Debinski, SB Tatter, Convection-enhanced delivery for the treatment of brain tumors. *Expert. review neurotherapeutics* **9**, 1519–1527 (2009).
3. CW Christine, et al., Magnetic resonance imaging–guided phase 1 trial of putaminal aadc gene therapy for parkinson's disease. *Annals neurology* **85**, 704–714 (2019).
4. MA Rogawski, Convection-enhanced delivery in the treatment of epilepsy. *Neurotherapeutics* **6**, 344–351 (2009).
5. L Crawford, J Rosch, D Putnam, Concepts, technologies, and practices for drug delivery past the blood-brain barrier to the central nervous system. *J. Control. Release* **240**, 251–266 (2016).
6. A Jahangiri, et al., Convection-enhanced delivery in glioblastoma: a review of preclinical and clinical studies. *J. neurosurgery* **126**, 1–10 (2016).
7. S Kunwar, et al., Phase iii randomized trial of ced of il13-pe38qqr vs gliadel wafers for recurrent glioblastoma. *Neuro-oncology* **12**, 871–881 (2010).
8. W Ehlers, A Wagner, Multi-component modelling of human brain tissue: a contribution to the constitutive and computational description of deformation, flow and diffusion processes with application to the invasive drug-delivery problem. *Comput. methods biomechanics biomedical engineering* **18**, 861–879 (2015).
9. R Raghavan, M Brady, Predictive models for pressure-driven fluid infusions into brain parenchyma. *Phys. medicine biology* **56**, 6179–204 (2011).
10. JH Kim, et al., Voxelized computational model for convection-enhanced delivery in the rat ventral hippocampus: Comparison with in vivo MR experimental studies. *Annals Biomed. Eng.* **40**, 2043–2058 (2012).
11. KH Støverud, M Darcis, R Helmig, SM Hassanizadeh, Modeling Concentration Distribution and Deformation During Convection-Enhanced Drug Delivery into Brain Tissue. *Transp. Porous Media* **92**, 119–143 (2012).
12. W Dai, et al., Voxelized model of brain infusion that accounts for small feature fissures: comparison with magnetic resonance tracer studies. *J. biomechanical engineering* **138** (2016).
13. C Nicholson, S Hrabětová, Brain extracellular space: the final frontier of neuroscience. *Biophys. journal* **113**, 2133–2142 (2017).
14. KE Holter, et al., Interstitial solute transport in 3d reconstructed neuropil occurs by diffusion rather than bulk flow. *Proc. Natl. Acad. Sci.* **114**, 9894–9899 (2017).
15. M Vidotto, D Botnariuc, E De Momi, D Dini, A computational fluid dynamics approach to determine white matter permeability. *Biomech. modeling mechanobiology* **18**, 1111–1122 (2019).
16. JP Kinney, et al., Extracellular sheets and tunnels modulate glutamate diffusion in hippocampal neuropil. *J. Comp. Neurol.* **521**, 448–464 (2013).
17. G Agustoni, et al., High resolution micro-computed tomography reveals a network of collagen channels in the body region of the knee meniscus. *Annals Biomed. Eng.* 10.1007/s10439-021-02763-6, 1–9 (2021).
18. J Maritz, G Agustoni, K Dragnevski, SP Bordas, O Barrera, The functionally grading elastic and viscoelastic properties of the body region of the knee meniscus. *Annals Biomed. Eng.* 10.1007/s10439-021-02792-1, 1–9 (2021).
19. A Bernardini, et al., Imaging and reconstruction of the cytoarchitecture of axonal fibres: enabling biomedical engineering studies involving brain microstructure. Submitted to *Communications Biology*, 10.21203/rs.3.rs-686577/v1 (2021).
20. T Duval, N Stikov, J Cohen-Adad, Modeling white matter microstructure. *Funct. neurology* **31**, 217 (2016).
21. A Abdollahzadeh, I Belevich, E Jokitalo, J Tohka, A Sierra, Automated 3d axonal morphometry of white matter. *Sci. reports* **9**, 1–16 (2019).
22. A Zaimi, et al., Axondeepseg: automatic axon and myelin segmentation from microscopy data using convolutional neural networks. *Sci. reports* **8**, 3816 (2018).
23. M Vidotto, et al., Fcnn-based axon segmentation for convection-enhanced delivery optimization. *Int. journal computer assisted radiology surgery* **14**, 493–499 (2019).
24. E Syková, C Nicholson, Diffusion in brain extracellular space. *Physiol. reviews* **88**, 1277–1340 (2008).
25. M Vidotto, D Dini, E De Momi, Effective diffusion and tortuosity in brain white matter in *2018 40th Annual International Conference of the IEEE Engineering in Medicine and Biology Society (EMBC)*. (IEEE), pp. 4901–4904 (2018).
26. BJ Jin, AJ Smith, AS Verkman, Spatial model of convective solute transport in brain extracellular space does not support a "glymphatic" mechanism. *The J. general physiology* **148**, 489–501 (2016).
27. K Hitti, S Feghali, M Bernacki, Permeability computation on a Representative Volume Element (RVE) of unidirectional disordered fiber arrays. *J. Comput. Math.* **34**, 246–264 (2016).
28. H Abdi, LJ Williams, Principal component analysis. *Wiley interdisciplinary reviews: computational statistics* **2**, 433–459 (2010).
29. G Franceschini, D Bigoni, P Regitnig, G Holzapfel, Brain tissue deforms similarly to filled elastomers and follows consolidation theory. *J. Mech. Phys. Solids* **54**, 2592 – 2620 (2006).
30. A Tavner, et al., On the appropriateness of modelling brain parenchyma as a biphasic continuum. *J. mechanical behavior biomedical materials* **61**, 511–518 (2016).
31. PA Netti, DA Berk, MA Swartz, AJ Grodzinsky, RK Jain, Role of extracellular matrix assembly in interstitial transport in solid tumors. *Cancer research* **60**, 2497–2503 (2000).
32. A Jamal, et al., Infusion mechanisms in brain white matter and their dependence on microstructure: An experimental study of hydraulic permeability. *IEEE Transactions on Biomed. Eng.* **68**, 1229–1237 (2021).
33. JP Basser, Interstitial Pressure , Volume, and Flow during Infusion into Brain Tissue. *Microvasc Res* **165**, 143–165 (1992).
34. AA Linninger, MR Somayaji, T Erickson, X Guo, RD Penn, Computational methods for predicting drug transport in anisotropic and heterogeneous brain tissue. *J. Biomech.* **41**, 2176–2187 (2008).
35. D Liewald, R Miller, N Logothetis, HJ Wagner, A Schüz, Distribution of axon diameters in cortical white matter: an electron-microscopic study on three human brains and a macaque. *Biol. Cybern.* **108**, 541–557 (2014).
36. L Zhang, M Yang, M Jiang, Mathematical modeling for convection-enhanced drug delivery. *Procedia Eng.* **29**, 268–274 (2012).
37. E Comellas, S Budday, JP Pelteret, GA Holzapfel, P Steinmann, Modeling the porous and viscous responses of human brain tissue behavior. *Comput. Methods Appl. Mech. Eng.* **369**, 113128 (2020).
38. A Bernardini, M Trovatelli, D Dini, EDEN2020 Ovine Brain Dataset for Imaging and Reconstruction of the Cytoarchitecture of Axonal Fibres. *Zenodo* 10.5281/zenodo.4772440, Version 1.0 (2021).
39. M Asgari, D De Zélicourt, V Kurtcuoglu, Glymphatic solute transport does not require bulk flow. *Sci. reports* **6**, 38635 (2016).
40. S Farina, S Claus, JS Hale, A Skupin, SP Bordas, A cut finite element method for spatially resolved energy metabolism models in complex neuro-cell morphologies with minimal remeshing. *Adv. Model. Simul. Eng. Sci.* **8**, 1–32 (2021).
41. PA Beaufort, C Geuzaine, JF Remacle, Automatic surface mesh generation for discrete models—a complete and automatic pipeline based on reparametrization. *J. Comput. Phys.* **417**, 109575 (2020).
42. X Yang, TJ Lu, T Kim, An analytical model for permeability of isotropic porous media. *Phys. Lett. Sect. A: Gen. At. Solid State Phys.* **378**, 2308–2311 (2014).
43. W Zhan, F Rodriguez y Baena, D Dini, Effect of tissue permeability and drug diffusion anisotropy on convection-enhanced delivery. *Drug delivery* **26**, 773–781 (2019).